CHEMISTRY OF MATERIALS

Open Access

pubs.acs.org/cm

Article

Hierarchical Self-Assembly of Disulfide-Linked Single-Stranded DNA into Stimuli-Responsive Pods

Volkan Kilinc,* Linawati Sutrisno, Joel Henzie, Emmanuel Picheau, Yusuke Yamauchi, Katsuhiko Ariga, and Jonathan P. Hill*

Cite This: *Chem. Mater.* 2026, 38, 1968−1979

Read Online

ACCESS | Metrics & More | Article Recommendations | Supporting Information

ABSTRACT: Controlling the large-scale assembly of charged biopolymers is a fundamental challenge in materials chemistry. Here, we report a chemical strategy that uses disulfide-linked single-stranded DNA (ssDNA) dimers as unique building blocks to drive the hierarchical self-assembly of functional DNA microstructures. Formed from short, random-sequence oligomers, these dimers first organize into DNA-salt composite nanobead condensates, which then serve as scaffolds for the assembly of uniform, microrod-shaped DNA condensates called DNA-pod condensates. The key innovation of this work is the material's unique, cooperative structural transition. Upon thermal stimulation (>60 °C), dsDNA-pod condensates undergo a rapid exfoliation into an expanded ssDNA network, a process driven by significant gains in configurational entropy and the relief of electrostatic repulsion. This establishes an accessible strategy for creating stimuli-responsive DNA materials through a chemistry-driven, sequence-independent pathway. We further demonstrate that these materials act as robust host matrices for encapsulating guest molecules like doxorubicin.

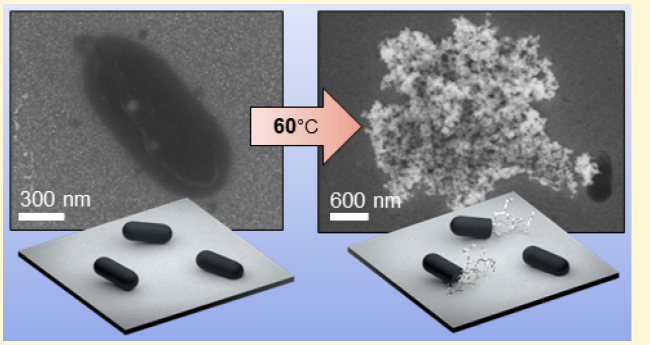

INTRODUCTION

Controlling the self-assembly of charged biopolymers like single-stranded DNA (ssDNA) into well-defined, functional microstructures is a fundamental challenge in materials chemistry. Current approaches rely primarily on either sequence-specific Watson−Crick base-pairing, which enables the creation of intricate static shapes including DNA origami,[1−3] or nonspecific condensation induced by multivalent cations.[5] While highly useful for the preparation of well-defined structures, these methods often require complex sequence design[4] or specific ionic conditions. An alternative strategy, using covalent yet dynamic chemical linkers to create unique building blocks for hierarchical assembly, remains less explored but offers a promising route to new material properties. Here, we introduce a chemical strategy that utilizes the disulfide bond as a covalent but conformationally flexible linker to guide the supramolecular organization of ssDNA. Unlike the rigid duplexes formed by hybridization, disulfide-linked ssDNA dimers possess a unique geometric constraint, a "kink", at the linkage point,[6] which frustrates simple linear polymerization and instead promotes condensation. While the aggregation of thiol-modified ssDNA has been observed,[7] a clear pathway to leverage this chemistry for creating ordered, stimuli-responsive microstructures has not been established. The central goal of this work is to elucidate such a pathway and characterize the functional material that results. To this end, we developed a straightforward, bottom-up self-assembly protocol for fabricating DNA-pod condensates: synthetic, microrod-shaped DNA condensates. The process begins with the reduction of a terminal disulfide protecting group on short (23−60 nt), randomly sequenced ssDNA to yield reactive ssDNA-SH. After purification using size-exclusion chromatography (SEC), these thiol-modified strands are oxidized under mild conditions to form ssDNA-S-S-ssDNA dimers. We demonstrate that these chemically distinct building blocks then spontaneously self-organize into uniform nanobead condensate intermediates, which subsequently serve as scaffolds for the hierarchical assembly of the final, micrometer-scale DNA-pod condensates architecture.

This manuscript details the synthesis and characterization of this subclass of DNA condensate material. We show that the DNA-pod condensates possess a stimuli-responsive function: upon thermal stimulation (>60 °C), double-stranded DNA-pod (dsDNA-pod) condensates form by sequential hybridization and undergo a rapid, cooperative structural exfoliation

Received: November 19, 2025
Revised: January 24, 2026
Accepted: January 28, 2026
Published: February 4, 2026

https://doi.org/10.1021/acs.chemmater.5c03128
Chem. Mater. 2026, 38, 1968−1979

into an expanded ssDNA network. This transition from a densely packed state is driven by entropic and electrostatic forces. As a proof-of-concept for the material's utility, we demonstrate its ability to encapsulate guest molecules, including doxorubicin (Dox). Finally, we conduct preliminary investigations into its interaction with preserved biological structures, revealing a preferential localization of encapsulated Dox within the nuclei of fixed cells. This work establishes an accessible chemical strategy for creating functional DNA materials, opening avenues for the design of stimuli-responsive systems from simple biopolymer precursors.

EXPERIMENTAL SECTION

General

Solvents and other materials were obtained from Tokyo Kasei Chemical Co. Ltd., Sigma-Aldrich Chemical Co. Ltd., Fujifilm Wako Chemical Co. Ltd., or Nacalai Tesque Chemical Co. Ltd., and were used as received.

Synthesis of DNA-pod Condensates

ssDNAs having randomly selected nucleotide sequences with lengths ranging from 23 nt to 60 nt were purchased from Integrated DNA Technologies (Coralville, USA). All sequences comprised a 3-hydroxypropyl disulfide modification at the 3′-terminal (ssDNA-CH_2−CH_2−CH_2−S-S-CH_2−CH_2−CH_2−OH) and optionally a 5′-terminal fluorophore with: fluorescein amidite (FAM), cyanine (Cy3) or Yakima yellow (YY). Sequences are annotated D1 to D11 for practical purposes (see Supplementary Table 1). All samples were ordered with prepurification by HPLC. ssDNA (D1 to D10) was diluted in PBS X-0.01 (containing Na^+, K^+, Cl^-, HPO_4^-, and PO_4^{2-}, Sigma-Aldrich) to obtain a solution of c = 20 μM. This solution (100 μL) was mixed with dithiothreitol (100 μL at 20 μM) at 45 °C for 10 min to cleave disulfide bonds. The solution was then passed through an SEC NAP DNA grade column (Cytiva) prepacked with Sephadex G-25 resin cross-linked dextran with epichlorohydrin and eluted with PBS X-0.01 (1.5 mL) to obtain a solution with c = 1.33 μM. The ssDNA-containing solution was then optionally mixed with an excess of its complementary ssDNA for 1 h at 50 °C. This solution was incubated at 25 °C for at least 48 h without stirring. An aliquot (40 μL) of the resulting solution was deposited on Si or Au substrate at 25 °C until evaporation followed by a rinsing step with deionized (DI) water to obtain a sample suitable for analysis.

Thermo-Stimulated Exfoliation of DNA-pod Condensates

dsDNA pods (400 μL, 1.33 μM) in PBS X-0.01 was heated for 10 min at temperatures in the range 60 to 100 °C then an aliquot (40 μL) was incubated on Au (with 5 nm chromium prelayer and 45 nm Au) or Si substrate at 25 °C for 24 h. Samples were then rinsed using DI water to remove excess salts.

Encapsulation of Guest Molecules in DNA-pod Condensates

DNA-pod condensates (100 μL, 1.33 μM; D1 to D9) were mixed with doxorubicin (Dox) (20 μM in DI water, 100 μL) or $TEA_8OxPBz_4Br_8$ (OxP, see Supplementary Figure 13) (20 μM in DI water, 100 μL) at 45 °C for 1 h without stirring. The solution was then passed through an SEC NAP DNA grade column prepacked with Sephadex G-25 resin (Cytiva) eluting with PBS X-0.01 (1.5 mL). The resulting solution was incubated at 25 °C for at least 48 h without stirring. An aliquot (40 μL) was deposited on Si or Au substrate at 25 °C until evaporation, followed by a rinsing step with DI water to obtain a sample suitable for analysis.

Scanning Electron Microscopy (SEM) and Energy-Dispersive X-ray Spectroscopy (EDX)

The surface morphologies of the obtained structures were investigated with scanning electron microscopy (SEM S-4800 Hitachi Co. Ltd.) operated at 5−15 kV. Elemental mapping using energy dispersive X-ray spectroscopy was performed by using a JEOL JSM-6010LA Analytical SEM operated at 15 kV.

Transmission Electron Microscopy (TEM) and EDX for Quantitative Analysis

Transmission electron microscopy measurements were performed on a JEOL-2100-F microscope or an FEI Talos F200X G2 microscope, both operated at an accelerating voltage of 200 kV. The ssDNA/DNA-pod condensates were deposited on a 12 nm-thick holey carbon film (Quantifoil) and initially imaged in scanning transmission electron microscopy (STEM) mode using a high-angle annular dark field (HAADF) detector. Simultaneously, the emitted X-rays were collected using energy-dispersive spectroscopy (EDX) to produce elemental maps for carbon, nitrogen, phosphorus, oxygen, sodium, sulfur and chlorine. High-resolution TEM (HRTEM) images were always collected after HAADF-STEM-EDX measurements. HRTEM altered the morphology of the bright spots in the microrods due to beam damage. In contrast, no significant morphological change was observed during HAADF-STEM imaging because the beam is scanned quickly with minimal dwell time, thus minimizing thermal damage.

Atomic Force Microscopy (AFM)

Topography and phase images of the DNA-pod condensates deposited on a silicon substrate were obtained using an AFM5000II (Hitachi) in tapping mode, using a Hitachi type SI-DF20 silicon cantilever ($f \sim$ 120 kHz, $C \sim$ 15 N/m) coated with aluminum.

Fluorescence Measurements

JASCO V870 fluorescence spectrophotometer equipped with a heat control system (JASCO ETC-273T) was used to obtain fluorescence spectra. The excitation wavelength was fixed at 495 nm, and the maximum emission wavelength was analyzed at 520 nm at different temperatures. A period of 5 min elapsed before each measurement.

Dynamic Light Scattering (DLS) and Zeta Potential Measurements

Both dimensions and surface potential analysis of ssDNA/DNA-pod condensates in solution were performed using a Photal ELS-Z Zeta-potential and Particle Size Analyzer instrument (Otsuka Electronics). Hydrodynamic radii were estimated by dynamic light scattering (photon correlation method) using a 1 cm^2 section quartz cuvette. Zeta potentials were measured by the laser Doppler method in a cell designed for diluted dispersions.

Cell Culture and Cell Lines

B164A5 cells (RCB0557, RRID: CVCL_4612) were purchased from the RIKEN Cell Bank (Tsukuba, Japan) and cultured in low-glucose Dulbecco's Modified Eagle Medium (DMEM) supplemented with 10% heat-inactivated fetal bovine serum (FBS; Gibco, Brazil) and 1% penicillin/streptomycin (Sigma-Aldrich). Cells were maintained in a humidified incubator at 37 °C with 5% CO_2. The culture

https://doi.org/10.1021/acs.chemmater.5c03128
Chem. Mater. 2026, 38, 1968−1979

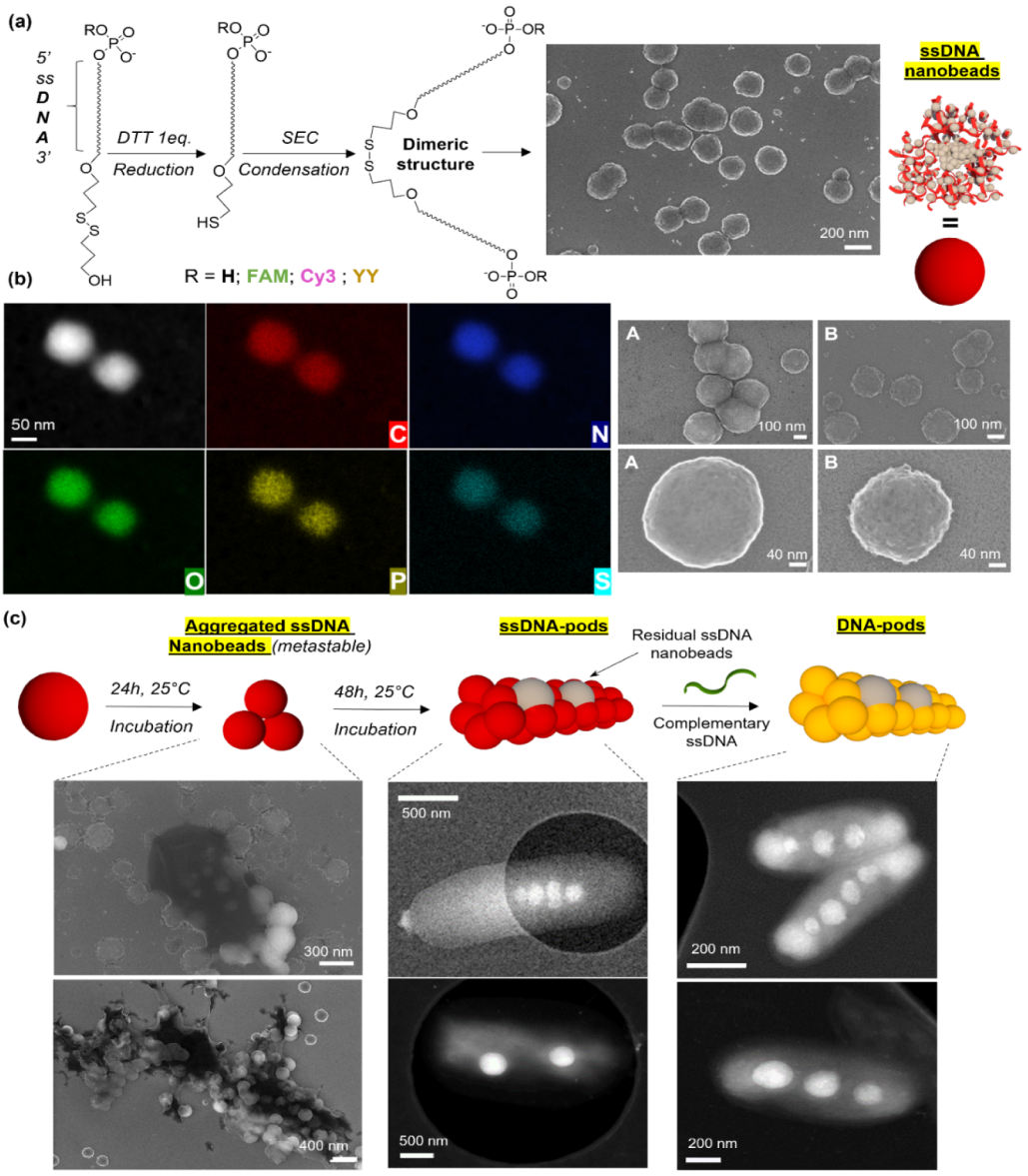

Figure 1. Formation sequence of synthetic DNA-pod condensates. (a) Schematic of ssDNA nanobeads condensate formation. Short ssDNA (≤60 nt) with a 3′-terminal cleavable disulfide moiety (ssDNA-S-S-R) and optional 5′-fluorophore (*R*' = H, FAM, Cy3, or YY) is treated with dithiothreitol (DTT) to yield ssDNA-SH. After purification of ssDNA-SH by size-exclusion chromatography (SEC), spontaneous oxidative dimerization occurs, forming ssDNA-S-S-ssDNA. These dimers then self-assemble into spherical ssDNA nanobeads. Representative SEM images show ssDNA nanobeads formed from sequences D3 and D2 (SEM panel A) and D1 (SEM panel B). (b) Representative HAADF-STEM image of an ssDNA nanobead (formed from 60 nt D3 ssDNA) showing a condensed core. Corresponding EDX elemental mapping confirms the presence of carbon (C), nitrogen (N), oxygen (O), phosphorus (P), and sulfur (S). (c) Hierarchical assembly of ssDNA nanobeads into ssDNA-pod condensates. SEM image (left) shows ssDNA nanobeads after ∼24 h incubation at 25 °C in PBS X-0.01, beginning to organize into larger structures. HAADF-STEM image (middle) shows a mature, rod-like ssDNA-pod condensates (containing bright spots, indicative of nanobead remnants) formed after ≥48 h incubation. These ssDNA-pod condensates can be subsequently hybridized with complementary ssDNA (e.g., at 50 °C) to form dsDNA-pod condensates (referred to generally as DNA-pods when context is clear). Morphologies shown are representative of at least three observations from two independent samples.

medium was replaced every 2 days, and cells were subcultured before reaching 80−90% confluency. Cell concentration was determined using Trypan Blue exclusion and measured with an automated cell counter (TC20, Bio-Rad Laboratories) and cell counting chambers. All reagents were handled under aseptic conditions and confirmed to be mycoplasma-free. The cell lines were routinely tested and verified to be free of mycoplasma contamination.

Confocal Microscopy Studies of DNA-pod Condensates Interactions with Fixed Cells

B164A5 cells (2×10^4 cells per compartment) were plated onto 35 mm glass-bottom dishes (Greiner Bio, 627870) and allowed to adhere overnight. The next day, they were gently rinsed with prewarmed PBS X-0.01, fixed with 4% paraformaldehyde, stained with Dox (20 μM), FAM labeled 60nt DNA-pod condensates (D10) with encapsulated Dox, FAM labeled 23nt DNA-pod condensates (D1) with encapsulated Dox, and Cy3 labeled 23nt DNA-pod con-

https://doi.org/10.1021/acs.chemmater.5c03128
Chem. Mater. 2026, 38, 1968−1979

densates (D8) with encapsulated Dox for 3 h, washed with PBS X-0.01, and observed under confocal microscopy (STELLARIS 8 DIVE, Leica). Cells stained with Hoechst 33342 (Dojindo, Japan) were excited at 405 nm, and emission was detected at 415−490 nm.

Guest $TEA_8OxPBz_4Br_8$ (OxP) Synthesis for Encapsulation

N_{21},N_{22},N_{23},N_{24}-Tetrakis(3,5-bis(bromomethyl)benzyl)-5,10,15,20-tetrakis(3,5-di-*t*-butyl-4-oxocyclohexadienylidene)-porphyrinogen(3,5-Br_2Bz)$_4$OxP was prepared according to a literature method. (3,5-Br_2Bz)$_4$OxP (1 g, 4.47×10^{-4} mol) and triethylamine (10 mL) were refluxed in dry acetonitrile (100 mL) for 24 h under a dry nitrogen atmosphere. Solvents and excess triethylamine were then removed under reduced pressure. The resulting dark green solid was triturated with tetrahydrofuran for 1 h and the resulting fine green powder was filtered and washed with tetrahydrofuran. The solid was dried for 48 h under reduced pressure and used without further purification in the subsequent experiments. Yield: 1.15 g (84%). 1H-NMR (D2O, 400 MHz, 298 K): δ = 7.89 (s, 4H, benzyl−Ar-H(4-position)), 7.66 (s, 8H, benzyl−Ar-H(2,6-positions)), 7.41−7.38 (m, 16H, meso-H and β-pyrrole-H), 5.02 (s, 8H, benzylic-CH_2-N), 4.40 (s, 16H, $-CH_2$-N$(Et)_3$), 3.41 (m, 48H, $-N(CH_2CH_3)_3$), 1.6−1.5 (m, 144H, $-N-(CH_2CH_3)_3$ and tBu-H) ppm. 13C NMR (D2O, 101 MHz, 298 K): δ = 186.09, 148.75, 139.44, 137.75, 135.68, 133.77, 133.58, 131.44, 131.13, 127.85, 124.19, 51.65, 45.85, 34.37, 28.02, 7.45, 6.32 ppm. FTIR (ATR): ν = 3417.2 (br. m, H_2O O−H str.), 2857.9 (m, C−H str.), 2909.9 (w, C−H str.), 2866.4 (w, C−H str.), 1586.6 (s, C═O str.), 1521.8 (m, C═C str.), 1483.9 (s, C−H def.), 1453.9 (s, C−H def.), 1402.7 (w), 1389.6 (w), 1361.1 (s), 1330.4 (w), 1305.5 (s), 1255.5 (m), 1223.9 (w), 1204.4 (w), 1182.9 (m), 1155.9 (w), 1136.6 (w), 1117.6 (w), 1089.0 (m), 1065.5 (m), 1043.6 (m), 1015.7 (m), 975.5 (m), 954.5 (m), 930.1 (w), 886.4 (m), 861.6 (w), 837.4 (w), 820.1 (w), 787.9 (br. m), 750.5 (w), 745.4 (m), 711.5 (m) cm^{-1}. The molecular ion could not be observed for this compound due to multiple charges and poor volatilization in the mass spectrometer. Further data about the synthesis conditions and characterization (Supplementary Figures 13−16) can be found in Supplementary Section 2.

RESULTS AND DISCUSSION

Design of DNA-Pod Condensates

The self-assembly of charged biopolymers into ordered, functional structures is a central theme in materials chemistry. Single-stranded DNA (ssDNA), a polyanion, is a particularly interesting building block due to its programmability and biocompatibility. However, its high charge density and conformational flexibility, with a persistence length of only ∼1−3 nm in physiological salt conditions,[8] mean that it does not spontaneously condense into discrete structures. Inducing collapse typically requires either sequence-specific hybridization[1−3] or charge neutralization with multivalent cations,[5] which can lead to uncontrolled precipitation. Our work explores an alternative chemical strategy: using a covalent, conformationally distinct linker to create a unique ssDNA building block that drives hierarchical assembly into well-defined microstructures.

To achieve this, we developed a strategy centered on the controlled dimerization of short ssDNA strands (<60 nt) through a disulfide bond. Unlike the rigid duplexes formed by base pairing, a disulfide bridge provides a covalent yet flexible linkage, introducing a unique geometric constraint into the ssDNA dimer.[6] We hypothesized that this "kinked" dimer architecture frustrates simple linear aggregation and instead favors a pathway of controlled condensation. Initially, ssDNA strands (23 and 60 nucleotides, random sequences D1−D11, Supplementary Table 1) modified at the 3′-terminus with a cleavable 3′-hydroxypropyl disulfide moiety (ssDNA-S-S-R) were treated with dithiothreitol (DTT) to yield reactive ssDNA bearing a terminal thiol group (ssDNA-SH). This mixture was immediately processed by size-exclusion chromatography (SEC) using a Sephadex G-25 column. The primary role of SEC in this step is to purify the ssDNA-SH oligomers by removing the small molecule reducing agents (DTT) and byproducts. Upon elution using dilute PBS X0.01 and removal of the DTT, the purified ssDNA-SH molecules undergo spontaneous oxidative dimerization to form stable ssDNA-S-S-ssDNA structures, facilitated by dissolved oxygen.[7]

These disulfide-bridged dimers behave very differently from free ssDNA under these conditions. While flexible ssDNA remains solvated due to electrostatic repulsion in low salt, the dimers spontaneously self-assemble at 25 °C into spherical, nanosized condensate structures, termed "DNA nanobeads" (Figure 1a). We attribute this condensation to the unique frustrated geometry imposed by the disulfide linker.[9] The covalent "kink" sterically hinders efficient, entropically favorable packing modes available to linear polymers, thus forcing the system toward an alternative energetic minimum: collapse into a condensed phase. This collapse maximizes favorable intermolecular interactions, including hydrophobic effects between bases, and optimizes counterion sharing, driven significantly by the entropic gain from releasing counterions upon condensation.[10,11] The formation of spherical nanobeads minimizes the unfavorable surface area exposure to the aqueous environment. Scanning electron microscopy (SEM) imaging reveals a median diameter for these nanobeads of 263 nm (range: 75 to 300 nm) for 60 nt ssDNA, while shorter 23 nt ssDNA yields an heterogeneous size distribution (range: 43 to 186 nm) (Supplementary Figure 1).

High-angle annular dark-field scanning transmission electron microscopy (HAADF-STEM) images suggest the nanobeads have a condensed, solid-like nature. Crucially, energy-dispersive X-ray spectroscopy (EDX) elemental mapping provides direct evidence supporting this condensation mechanism (Figure 1b). The analysis confirms the presence of the expected elements of the dimeric DNA (C, N, O, P, S). However, a heterogeneous distribution of phosphorus (P) relative to oxygen (O) and the presence of sodium (Na) (Supplementary Figure 2) indicates that the DNA nanobeads are not pure DNA, but rather are coassembled with phosphate salts from the buffer. This coassembly effectively lowers the net charge density within the condensate, further stabilizing the structure and explaining its formation under otherwise electrostatically unfavorable low-salt conditions.

Further incubation of these composite DNA nanobead condensates at 25 °C under quiescent conditions promotes their hierarchical assembly into distinctive, elliptical, micro-sized rod condensate structures, which we term "DNA-pods" (Figure 1c). While the precise forces driving this secondary ordering require further investigation, it highlights a complex, multistep assembly pathway initiated by the specific chemistry of the disulfide linker. This multistep hierarchical assembly is critically dependent on a specific set of chemical and physical parameters, as demonstrated by a series of control experiments

https://doi.org/10.1021/acs.chemmater.5c03128
Chem. Mater. 2026, 38, 1968−1979

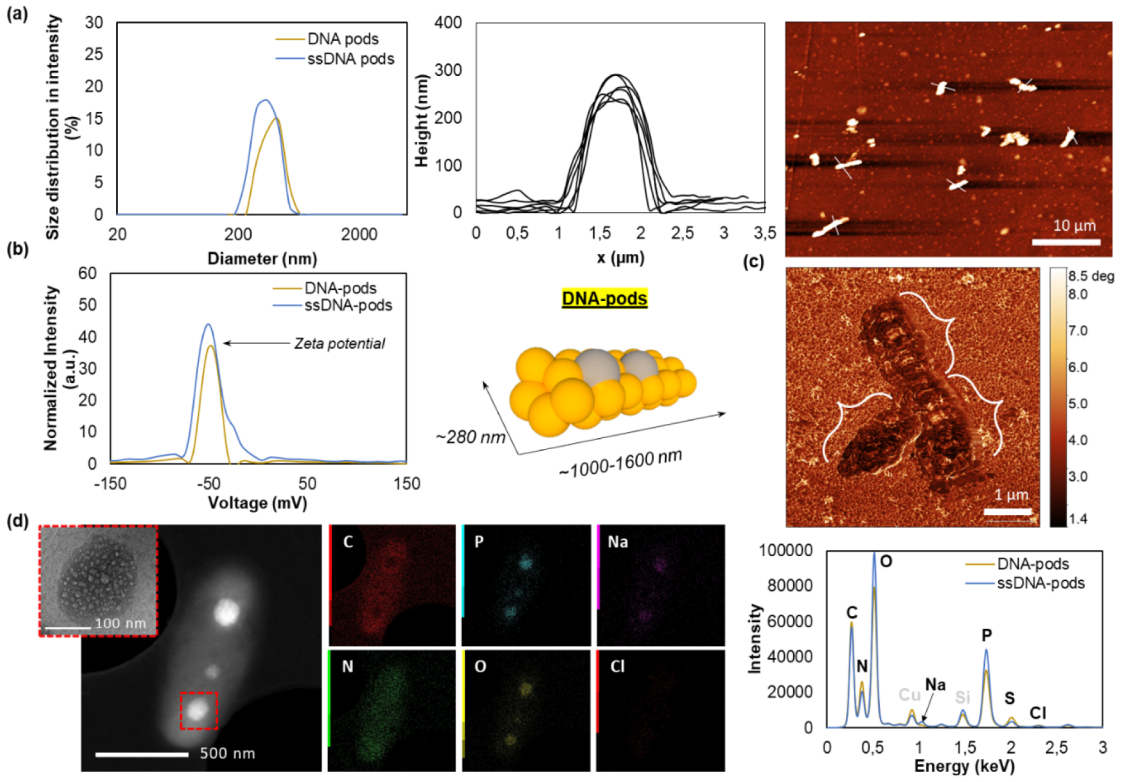

Figure 2. Characterization of DNA-pods. (a) Size characterization of ss/dsDNA-pods. DLS measurements provide the average effective hydrodynamic size (likely reflecting rod width/cross-section) in dispersion. AFM images (representative example shown) allow visualization of morphology and dimensions (N pods = 6). (b) Colloidal stability assessment. Zeta potential measurements for DNA-pods (both ssDNA- and dsDNA-forms) show a strong negative surface charge (typically ~− 50 mV, corresponding to an electrophoretic mobility of ~4×10^{-4} $cm^2/V{\cdot}s$), indicative of good dispersion stability. (c) AFM phase image of DNA-pods revealing a dense, solid internal structure, inconsistent with a hollow core. (d) HAADF-STEM image of an ssDNA-pod structure with bright spots at its interior. The inset image shows the HRTEM image of the bright spot located in the red box. The bright spots correspond to regions of higher density, likely crystalline phosphate deposits. EDX elemental mapping show C, N, P, O, Na and Cl. The spots show high concentrations of P and O, a small quantity of Na and deficiency of C. EDX spectrum of ssDNA/DNA pods is shown at bottom right. Absence of Cl indicates efficient rinsing.

(Supplementary Figure 3). The formation of well-defined nanobeads, the primary building block, is contingent upon the presence of the 3′-thiol modification; ssDNA lacking this group (D11) only forms an amorphous condensate (Supplementary Figure 3d). Similarly, the size-exclusion chromatography step is essential. Attempts to form nanobeads without it were unsuccessful (Supplementary Figure 3e), which confirms the crucial role of this step in purifying the reactive ssDNA-SH dimers from DTT to allow for the subsequent oxidative assembly pathway. Furthermore, the process is highly sensitive to the physical and chemical environment. Well-defined structures do not form at higher incubation temperatures (e.g., 45 °C, Supplementary Figure 3a), at high initial ssDNA concentrations (>10 μM, Supplementary Figure 3b), with continuous stirring (Supplementary Figure 3c), or in buffers with high ionic strength (e.g., PBS X-1) or different compositions (e.g., Tris-HCl) (Supplementary Figure 3f,g). Conversely, the underlying self-assembly process is notably tolerant to variations in ssDNA sequence composition (Supplementary Figure 3i), 5′-modifications (e.g., FAM, Cy3, YY) (Supplementary Figure 3h), and DNA length (up to 60 nt) (Supplementary Figure 3j). This highlights that the assembly is a robust, chemistry-driven, sequence-independent fabrication method that requires a precisely controlled set of physical conditions.

Characterization of DNA-pod Condensates

The morphology and physicochemical properties of the DNA-pod condensates were comprehensively characterized to validate their structure and composition. Dynamic light scattering (DLS) of DNA-pods dispersed in dilute PBS X-0.01 indicates an average hydrodynamic size of approximately 280 nm (Figure 2a). Given their rod-like morphology, this DLS value reflects the effective cross-sectional dimension of the solvated structures. This was corroborated by imaging using atomic force microscopy (AFM) and SEM, which confirm a uniform, solid rod-shaped morphology with lengths of 1000−1600 nm and a consistent diameter.

The colloidal stability of the DNA-pod condensates dispersion was assessed by zeta potential measurements, which reveal a strongly negative surface charge of approximately −50 mV for pods made from either ssDNA or dsDNA. This high surface charge results in colloidal stability, preventing aggregation for over one year in PBS X-0.01 at room temperature (Figure 2b). AFM phase imaging further confirms that the pods possess a dense internal structure, ruling out a hollow, tube-like morphology (Figure 2c).

Elemental composition was investigated using EDX. Typical spectra of ssDNA-pods reveal the expected signals for carbon (C; 0.28 keV), nitrogen (N; 0.39 keV), oxygen (O; 0.52 keV), phosphorus (P; 2.0 keV), and a weak peak for sulfur (S; 2.3 keV) corresponding to the 3′-end disulfide linkage (Figure 2d).

https://doi.org/10.1021/acs.chemmater.5c03128
Chem. Mater. 2026, 38, 1968−1979

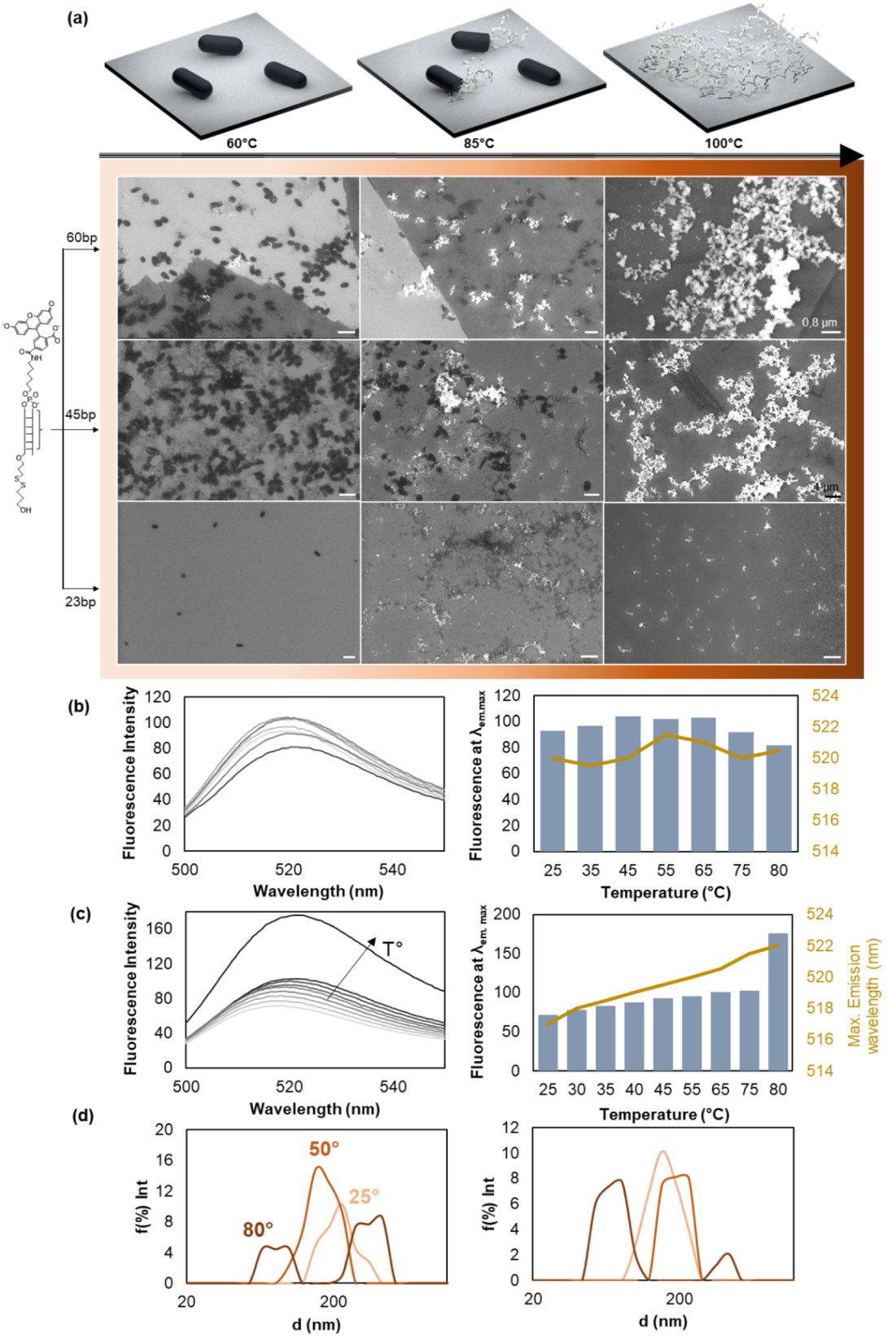

Figure 3. Structure transition capability of the DNA-pods. (a) Thermally induced exfoliation of dsDNA-pods. SEM images show dsDNA-pods (formed from D1, D7, or D10 sequences, incorporating a 5′-FAM fluorophore) after 10 min incubation at indicated temperatures (60 °C, 85 °C, 100 °C). Exfoliation into a networked DNA structure is evident at temperatures ≥60 °C. Scale bar = 2 μm (unless specified). (b) Fluorescence monitoring of thermal exfoliation. Control experiment using 5′-FAM-labeled D5 ssDNA-pods in PBS X-0.01. Changes in FAM emission intensity and maximum emission wavelength (excitation at 495 nm) are shown as a function of temperature. No significant exfoliation-related fluorescence changes. (c) Thermal exfoliation of 5′-FAM-labeled D5 dsDNA-pods in PBS X-0.01 under identical conditions. Sharp increase of fluorescence

https://doi.org/10.1021/acs.chemmater.5c03128
Chem. Mater. 2026, 38, 1968−1979

Figure 3. continued

emission intensity is observed. (d) DLS measurements of 5′-FAM-labeled D7 and D10 dsDNA at 25, 50, and 80 °C. Diameter alteration of DNA-pods induced by the exfoliation is observed at 80 °C.

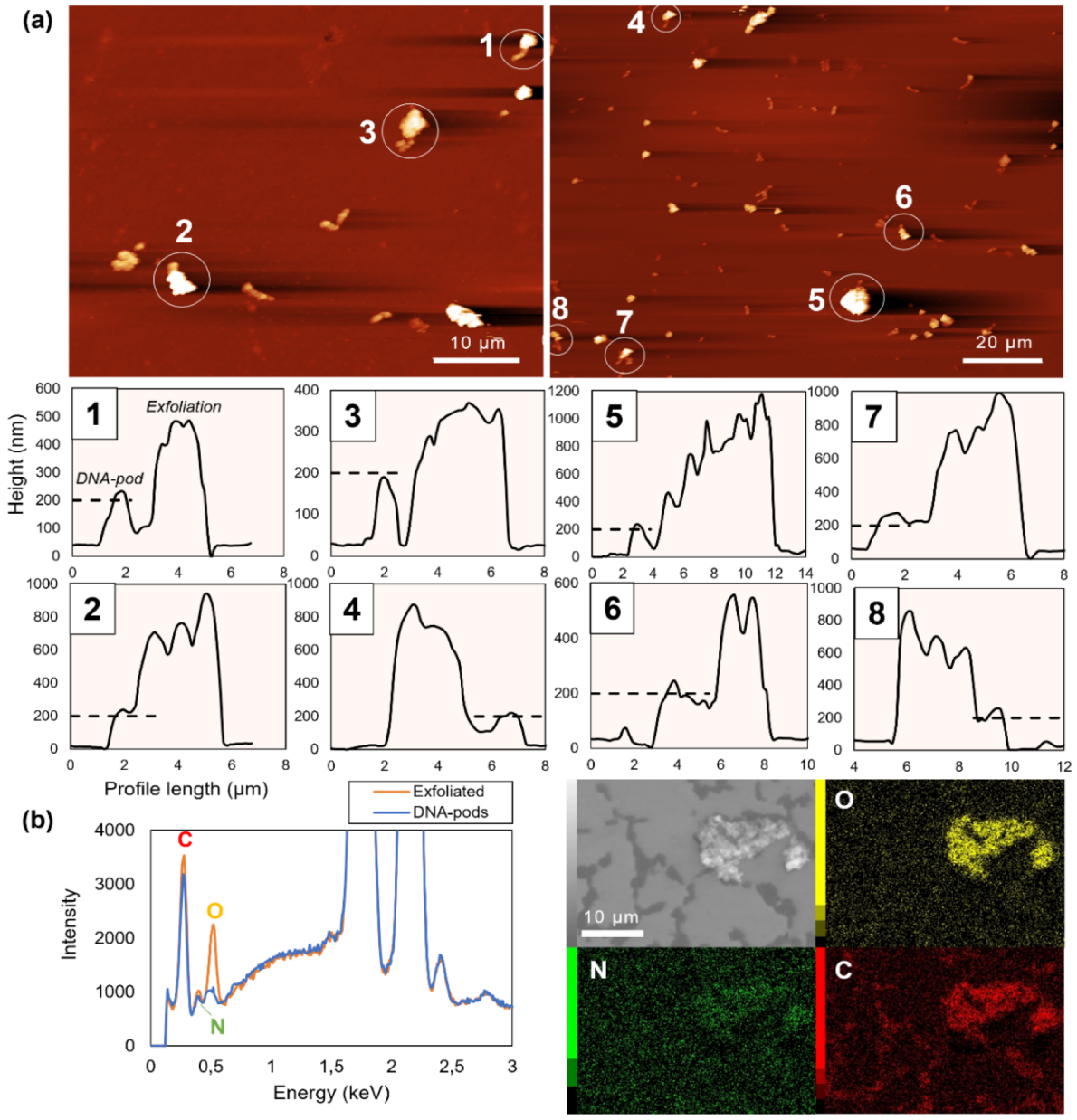

Figure 4. Structure transition of the DNA-pods. (a) AFM analysis of exfoliated dsDNA-pods (originally formed from D1 dsDNA). Representative topography images and corresponding height profiles (N = 8 examples) show significant volumetric expansion upon exfoliation. A dashed line at ~200 nm (typical initial pod height) provides a visual reference. The average volumetric expansion ratio was calculated as 8.4 (range: 2.5−21). (b) SEM-EDX comparison of compact dsDNA-pods (pre-exfoliation) and the exfoliated ssDNA network. The exfoliated material exhibits a relative increase in oxygen and phosphorus signals, consistent with greater DNA backbone exposure.

A residual sodium (Na) signal at 1.04 keV was also detected, consistent with the phosphate salt coassembly observed during nanobead formation, while the general absence of chlorine (Cl; 2.62 keV) confirms effective removal (by rinsing) of any NaCl present during sample preparation. HAADF-STEM imaging further reveals the presence of several bright, electron-dense spots within some DNA-pod condensates. EDX elemental mapping correlates these spots with regions that are rich in P, Na, and O but low in C. High-resolution TEM of these areas shows a porous, beam-sensitive material (inset, Figure 2d), identified as remnants of the phosphate-rich nanobead scaffold from which the DNA-pods assemble. Notably, not all DNA-pod condensates display these bright spots with the same intensity or frequency (Supplementary Figure 4), indicating variability in the extent of nanobead remnant incorporation or their subsequent reorganization within the mature DNA-pod structure.

https://doi.org/10.1021/acs.chemmater.5c03128
Chem. Mater. 2026, 38, 1968−1979

Another finding is the ability to chemically tune the composition of the material post-assembly. When the ssDNA-pods were converted to dsDNA-pods by hybridization with complementary strands, EDX analyses indicate a marked reduction in the P, O, and Na signal intensities relative to the carbon signal. This indicates that the formation of the more rigid, ordered dsDNA duplexes within the pod induces a structural rearrangement that expels the coassembled sodium phosphate salts. This transition from a composite to a more purely DNA-based material demonstrates that Watson−Crick hybridization can override the initial self-assembly interactions. The combination of a defined morphology, robust colloidal stability, and the capacity for post-assembly compositional tuning establishes DNA-pod condensates as a versatile platform for creating functional biopolymer materials.

Structure Transition of DNA-pod Condensates

A key characteristic of the DNA-pod condensates material is its capacity for large-scale, stimuli-responsive structural transitions. We investigated this property by first converting the ssDNA-pods into a dsDNA state by hybridization with complementary strands. These dsDNA-pods exhibit a distinct temperature-responsive behavior. Upon heating above 60 °C, they undergo a sharp structural transition, disassembling from compact rods into an expanded, networked structure (Figure 3a). This exfoliation phenomenon is exclusive to the dsDNA-pods; control experiments using the initial ssDNA-pods showed no such transition under identical conditions (Supplementary Figure 5), confirming that the process is coupled to the presence of the DNA duplex. The process was also found to be largely independent of the dsDNA length (within the 23−60 bp range tested), sequence, or the presence of 5′-modifications on the original strands (Supplementary Figure 6).

The exfoliation was first monitored using fluorescence emission spectroscopy of dsDNA-pods incorporating 5′-FAM labeled DNA strands (Figure 3c). As the temperature increased, the FAM emission maximum gradually shifted from 518.0 to 521.5 nm, indicating a red shift (bathochromic shift) which is interpreted as a microenvironmental change of the fluorophore due to the structural relaxation of the DNA micropods. This phenomenon is accompanied by a slight increase in fluorescence intensity below 70 °C, attributed to minor conformational adjustments or release of screening ions. Critically, a sharp increase in FAM emission intensity was observed between 75−80 °C, pinpointing the primary exfoliation temperature. This pronounced intensity increase is indicative of FAM de-quenching as the DNA duplexes melt and the condensed pod structure disassembles, leading to greater separation between fluorophores and DNA bases and increased solvent exposure. In contrast, control experiments with ssDNA-pods showed no significant redshift or fluorescence emission variation across the same temperature range, confirming the dsDNA-dependent nature of this exfoliation (Figure 3b). DLS measurements of dsDNA-pod diameters while applying temperature stress-test (Figure 3d) showed clear alteration of the initial uniform size distribution of the micropods at 80 °C, confirming the exfoliation of the material.

AFM profilometry corroborates this large-scale structural change, revealing that exfoliated dsDNA-pods expand significantly, with an average volumetric expansion ratio of 8.4 (range: 2.5−21) compared to their initial height of ∼200 nm (Figure 4a). The exfoliated material forms a network of ssDNA strands with observable pores (e.g., ∼30 nm for D1-derived DNA-pods[12]). EDX chemical elemental mapping of these exfoliated networks (Figure 4b, Supplementary Figure 7) shows relatively increased oxygen and phosphate signals compared to compact dsDNA-pods, consistent with the greater exposure of the DNA backbone upon dehybridization and network expansion. Given that disulfide bonds are stable under these thermal conditions, the exfoliated network is understood to be composed of the original ssDNA−S-S-ssDNA dimeric strands along with their released complementary ssDNA strands. Preliminary results from a few samples showed possible reversibility of the thermal exfoliation upon cooling (Supplementary Figure 8). However, the cooling process requires optimization to obtain a higher population of reversed DNA-pods.

While a temperature trigger exceeding 60 °C is supraphysiological, it is fully compatible with established clinical and preclinical strategies for inducing localized hyperthermia. Techniques such as High-Intensity Focused Ultrasound (HIFU) can noninvasively heat deep regions of tissue to precise ablative temperatures (>60 °C) with high spatial resolution.[13] This provides a clear potential pathway for externally triggering the exfoliation of DNA-pods on-demand at a target site. This mechanism could also be integrated with photothermal therapy (PTT) or magnetic hyperthermia, where colocalized nanoparticles generate heat upon external stimulation.[14] We propose that this exfoliation is a cooperative structural transition driven by physicochemical forces unleashed upon dsDNA melting. The primary driving force is a gain in configurational entropy. The transition from a condensed matrix of relatively rigid dsDNA segments to a network of highly flexible ssDNA chains represent a substantial increase in the system's accessible conformational states. This entropic gain is coupled with a sharp increase in intramolecular electrostatic repulsion within the now unshielded and flexible polyanionic ssDNA strands. Together, these entropic and electrostatic forces overcome the cohesive interactions holding the pod together, driving its rapid and extensive expansion. This cooperative disassembly from a densely packed state is conceptually reminiscent of genome ejection mechanisms in some bacteriophages.[15,16] The resulting highly exposed ssDNA network is a chemically distinct material, with a reactive nature that has been noted previously for sensing applications.[12]

Drug Encapsulation by DNA-pod Condensates

Having established the synthesis and unique structural properties of the DNA-pods, we next investigated their capabilities as a host matrix for molecular encapsulation. The condensed, DNA-rich internal environment of the pods presents a distinct microenvironment for host−guest interactions.[17−19] To explore this, we selected two model guest molecules with different physicochemical properties: doxorubicin (Dox), a well-known DNA intercalator, and a larger, synthetic cationic macromolecule, OxP (see Supplementary Section 2 for synthesis and properties).

Prior to encapsulation studies, highly sensitive EDX mapping of empty DNA-pods condensates (Supplementary Figure 9) was performed. This analysis distinguished between nodular regions, previously identified as remnants of the phosphate-rich nanobead scaffold (characterized by higher O and P signals), and interspace areas, which are richer in DNA (higher C and N signals from nucleobases). While effective rinsing was performed, some residual sodium associated with

https://doi.org/10.1021/acs.chemmater.5c03128
Chem. Mater. 2026, 38, 1968−1979

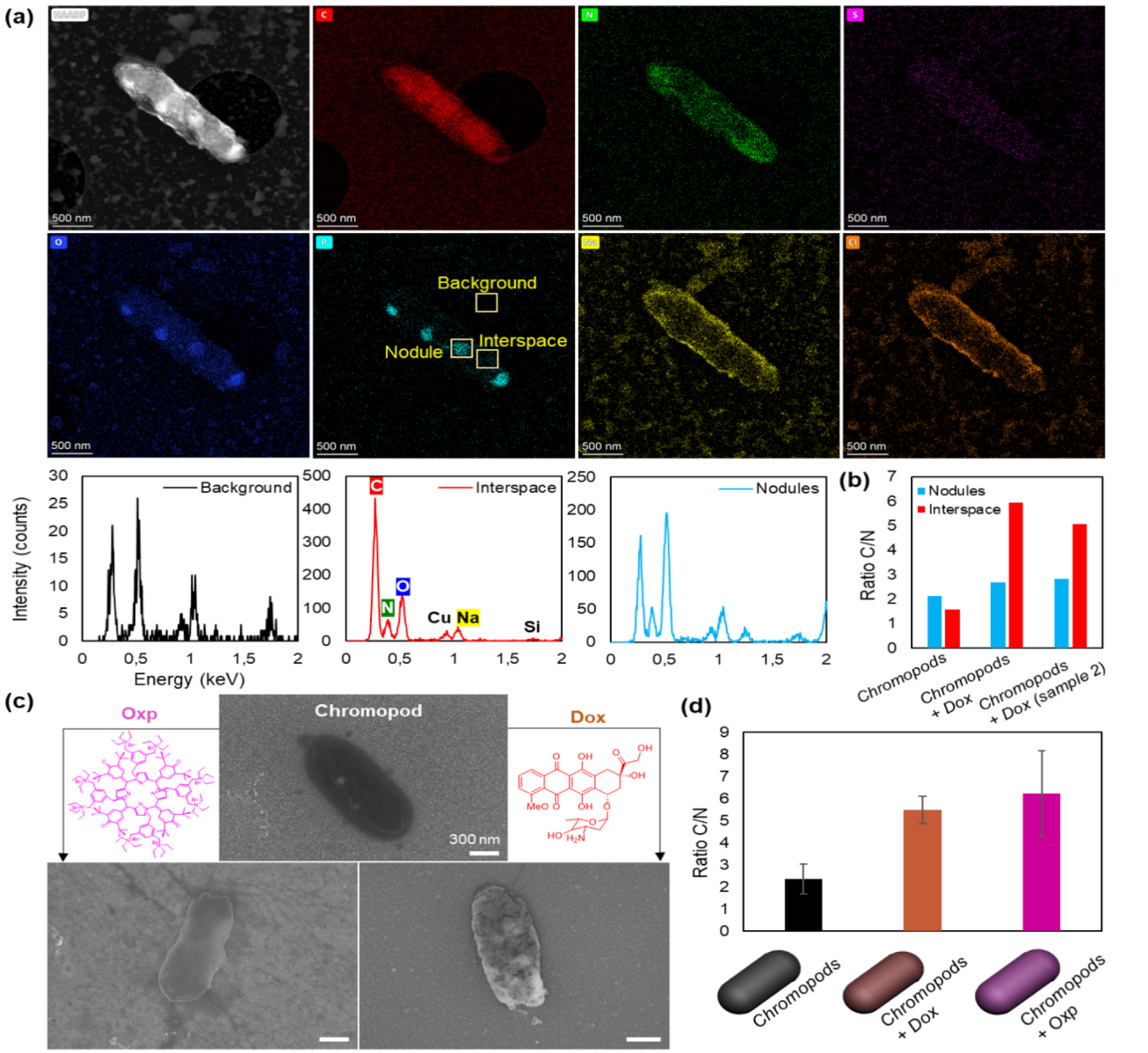

Figure 5. Encapsulation of functional molecules by DNA-pods. (a) HAADF-STEM image and EDX elemental mapping (C, N, O, S, P, Na, Cl) of DNA-pods after incubation with doxorubicin. Nodules rich in P and O (phosphate residue from nanobeads scaffold) are observed. Spectra of background, interspace and nodules inside DNA-pods are shown. Pods are coated with NaCl. (b) Preferential localization of doxorubicin within DNA-pods. Comparison of C/N atomic ratios in interspace areas and nodular regions before (empty) and after Dox encapsulation, indicating Dox enrichment in interspace areas. (c) Enhanced SEM contrast in DNA-pods after encapsulation of doxorubicin (Dox) or OxP, indicative of successful loading. (d) Overall increase in C/N atomic ratio for DNA-pods after encapsulation of Dox or OxP compared to empty pods (theoretical DNA C/N ≈ 2.45), confirming guest molecule incorporation.

phosphate from the buffer could be observed, consistent with the coassembly process.

A key insight into the material's dynamic nature was revealed during the encapsulation process. When preformed DNA-pod condensates were mixed with an excess of a guest molecule and then purified using SEC, the material was observed to transiently revert to nanobead-like structures. These drug-loaded nanobeads then reassemble into mature, drug-loaded DNA-pods following a 48-h incubation period. This dynamic disassembly and reassembly behavior indicates that the host−guest interactions involved are robust and maintained within the core nanobead components even during macroscopic structural rearrangement. Following encapsulation of Dox within reassembled DNA-pods, we used EDX mapping to characterize the location of the guest molecules within the host architecture (Figure 5a, Supplementary Figure 10). To qualitatively assess and localize the encapsulated molecules, we analyzed changes in the local carbon-to-nitrogen (C/N) atomic ratios, leveraging the different elemental compositions of the guest molecules compared to DNA. For instance, the theoretical C/N ratio for the DNA sequences used is ∼2.4−2.5, while Dox has a higher C/N ratio. An increase in the measured C/N ratio within specific regions of the DNA-pods postencapsulation therefore indicates local enrichment of the guest molecule. Indeed, EDX analysis revealed significantly elevated C/N ratios, particularly in the interspace areas of Dox- loaded DNA-pods (Figure 5b), compared to empty pods (C/N ratio of ∼2.45, consistent with

https://doi.org/10.1021/acs.chemmater.5c03128
Chem. Mater. 2026, 38, 1968−1979

theoretical DNA values). This indicates preferential loading of Dox within these DNA-rich regions, facilitated by mechanisms such as intercalation or groove binding. This finding is further supported by brighter contrast in these areas in SEM images of Dox-loaded pods (Figure 5c). Overall, the C/N ratio in Dox-loaded pods increased significantly (Figure 5d, Supplementary Figure 11a), confirming Dox encapsulation.

Encapsulation of the cationic OxP molecule was characterized by a marked reduction in the DNA-pod zeta potential from approximately −47 mV to −16 mV (Supplementary Figure 11b). This significant charge neutralization provides clear evidence of a strong electrostatic interaction between the anionic DNA host matrix and the cationic guest. Furthermore, when OxP-loaded DNA-pods are subjected to acid-induced structural transition, the characteristic purple color of OxP remained visibly associated with the resulting DNA aggregates (Supplementary Figure 11c). This observation demonstrates the excellent stability of this host−guest complex, showing that the guest molecule is retained even when the macroscopic morphology of the host material is completely altered. Together, these results establish DNA-pod condensates as a robust and dynamic host matrix capable of encapsulating diverse guest molecules through different interaction mechanisms.

Interaction of DNA-pod Condensates with Fixed Cellular Scaffolds

To characterize the interaction of the DNA-pod material and its cargo with complex biological substrates, we examined the distribution of encapsulated guest molecules within PFA-fixed B164A5 murine melanoma skin cancer cells. This experiment probes the affinity and partitioning behavior of the material within a preserved cellular architecture. When fixed cells were incubated with a solution of free doxorubicin (Dox), the drug exhibited a widespread distribution only throughout the fixed cytoplasm (nuclear-to-cytoplasmic fluorescence ratio = 0.02) (Figure 6a). In contrast, when the cells were incubated with Dox encapsulated within DNA-pods, confocal microscopy reveals that the Dox fluorescence is primarily accumulated in the nuclear regions, showing strong colocalization with the DNA-specific Hoechst 33342 stain (nuclear-to-cytoplasmic fluorescence ratio = 0.72−0.97) (Figure 6b-d). This observation indicates that the DNA-pod condensates formulation alters the partitioning behavior of Dox within this nonliving system, leading to a higher concentration or retention within the preserved nuclear structures. Interestingly, this effect is guest-dependent. When fixed cells were incubated with DNA-pods loaded with the cationic macromolecule OxP, the guest molecule was located predominantly in the cytoplasmic regions (Supplementary Figure 12).

These studies provide insights into the host−guest interactions between the DNA-pod condensates and a complex biological substrate. The differing distribution patterns highlight that the physicochemical properties of the guest molecule significantly influence its ultimate localization. While these findings do not demonstrate active cellular uptake, the preferential nuclear association of Dox warrants further investigation in live-cell models.

CONCLUSION

This work describes a chemical strategy for the bottom-up fabrication of functional DNA-based materials. We have demonstrated that disulfide-linked ssDNA dimers, formed from short, randomly sequenced oligomers, serve as unique building blocks for a robust, hierarchical self-assembly pathway. This process first yields DNA-salt composite nanobead condensates, which then organize into uniform, microrod-shaped condensate structures termed DNA-pods.

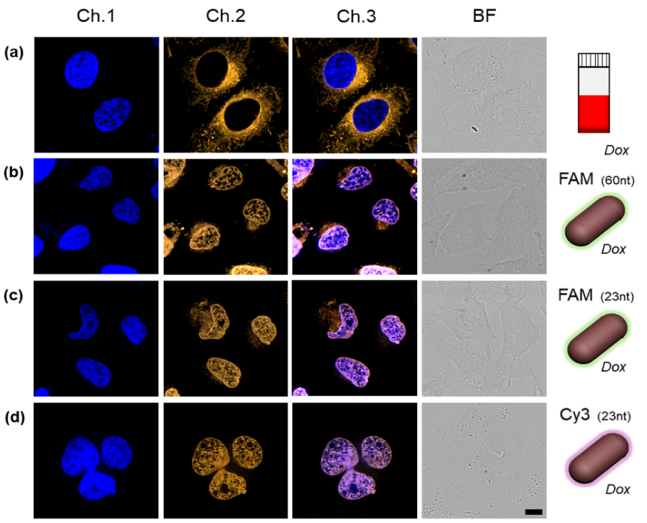

Figure 6. Distribution of doxorubicin in fixed B164A5 cells after incubation with DNA-pods. Fluorescent microscope images of B164A5 skin cancer cells, fixed, and incubated with (a) Dox solution at 20 μM, (b) FAM labeled 60nt DNA-pods (D10) with encapsulated Dox, (c) FAM labeled 23 nt DNA-pods (D1) with encapsulated Dox, and (d) Cy3 labeled 23 nt DNA-pods (D8) with encapsulated Dox. Ch.1 corresponds to excitation/emission at 405/415−490 nm of Hoechst 33342 (used as reference), Ch. 2 to 520/530−560 nm and Ch. 3 as merge of Ch. 2 and 3. BF are bright field confocal microscope images. Calculated nuclear-to-cytoplasmic fluorescence ratio are respectively 0.02, 0.72, 0.88, and 0.97 for (a), (b), (c), and (d). Scale bar = 10 μm.

The key contribution of this work is the demonstration that these materials possess a cooperative structural transition. Upon thermal stimulation (>60 °C), dsDNA-pods undergo a rapid exfoliation into an expanded ssDNA network, a process driven by a gain in configurational entropy and the relief of electrostatic repulsion upon DNA duplex melting. This thermal trigger is notably compatible with clinically relevant hyperthermia techniques like HIFU, indicating a clear pathway for the external control of the material's state in future applications.

As a functional material, DNA-pods act as a robust host matrix, capable of encapsulating diverse guest molecules like doxorubicin through a dynamic disassembly and reassembly process. Although the controlled release of the drugs has not been demonstrated here, the preliminary studies on fixed cellular scaffolds revealed that the DNA-pod condensates formulation influences the partitioning of its cargo, leading to a preferential nuclear association for encapsulated doxorubicin.

In summary, we have presented a simple and scalable method to create a stimuli-responsive, biopolymer-based material. The use of a specific chemical linker to control a complex, hierarchical self-assembly cascade represents an alternative tool for materials chemists. DNA-pod condensates are a versatile platform enabling the design of advanced functional DNA materials for applications in materials science and bionanotechnology.

https://doi.org/10.1021/acs.chemmater.5c03128
Chem. Mater. 2026, 38, 1968−1979

■ ASSOCIATED CONTENT

Supporting Information

The Supporting Information is available free of charge at https://pubs.acs.org/doi/10.1021/acs.chemmater.5c03128.

Table of DNA materials and additional experimental details and methods, including microscope photographs of the DNA material structure and NMR data of the OxP synthesized compound (PDF)

■ AUTHOR INFORMATION

Corresponding Authors

Volkan Kilinc − *Research Center for Materials Nanoarchitectonics (WPI-MANA), National Institute for Materials Science (NIMS), Tsukuba, Ibaraki 305-0044, Japan;* orcid.org/0009-0006-4402-1024; Email: contact@researchvyk.com

Jonathan P. Hill − *Research Center for Materials Nanoarchitectonics (WPI-MANA), National Institute for Materials Science (NIMS), Tsukuba, Ibaraki 305-0044, Japan;* orcid.org/0000-0002-4229-5842; Email: jonathan.hill@nims.go.jp

Authors

Linawati Sutrisno − *Research Center for Materials Nanoarchitectonics (WPI-MANA), National Institute for Materials Science (NIMS), Tsukuba, Ibaraki 305-0044, Japan;* orcid.org/0000-0003-3085-9660

Joel Henzie − *Research Center for Materials Nanoarchitectonics (WPI-MANA), National Institute for Materials Science (NIMS), Tsukuba, Ibaraki 305-0044, Japan*

Emmanuel Picheau − *Research Center for Materials Nanoarchitectonics (WPI-MANA), National Institute for Materials Science (NIMS), Tsukuba, Ibaraki 305-0044, Japan*

Yusuke Yamauchi − *Australian Institute for Bioengineering and Nanotechnology (AIBN), The University of Queensland, Brisbane QLD 4072, Australia; Department of Advanced Materials Process Engineering, Graduate School of Engineering, Nagoya University, Nagoya, Aichi 464-8601, Japan; Department of Chemical and Biomolecular Engineering, Yonsei University, Seoul 03722, South Korea;* orcid.org/0000-0001-7854-927X

Katsuhiko Ariga − *Research Center for Materials Nanoarchitectonics (WPI-MANA), National Institute for Materials Science (NIMS), Tsukuba, Ibaraki 305-0044, Japan; Graduate School of Frontier Sciences, The University of Tokyo, Kashiwa 277-8561, Japan;* orcid.org/0000-0002-2445-2955

Complete contact information is available at: https://pubs.acs.org/10.1021/acs.chemmater.5c03128

Author Contributions

The manuscript was written through the contributions of all authors. All authors have given their approval to the final version of the manuscript.

Funding

This work was supported by funding from the Postdoctoral Fellowship of Japan Society for the Promotion of Science program (JSPS). This work was partly supported by the World Premier International Research Center Initiative (WPI Initiative), MEXT, Japan. The authors are grateful to the JST-ERATO Yamauchi Materials Space Tectonics Project (JPMJER2003) and the Queensland Node of the Australian National Fabrication Facility (ANFF-Q). The authors are grateful to the Japan Society for the Promotion of Science for support through JP25H00898 (K.A.) and 20K05453 (J.H.).

Notes

The authors declare no competing financial interest.

■ REFERENCES

(1) Seeman, N. C. Nucleic Acid Junctions and Lattices. *J. Theor. Biol.* **1982**, *99* (2), 237−247.

(2) Winfree, E.; Liu, F.; Wenzler, L. A.; Seeman, N. C. Design and Self-Assembly of Two-Dimensional DNA Crystals. *Nature* **1998**, *394*, 539−544.

(3) Rothemund, P. W. K. Folding DNA to Create Nanoscale Shapes and Patterns. *Nature* **2006**, *440* (7082), 297−302.

(4) Simmel, F. C.; Yurke, B.; Singh, H. R. Principles and Applications of Nucleic Acid Strand Displacement Reactions. *Chem. Rev.* **2019**, *119* (10), 6326−6369.

(5) Widom, J.; Baldwin, R. L. Cation-Induced Toroidal Condensation of DNA Studies with Co3+(NH3)6. *J. Mol. Biol.* **1980**, *144*, 431−453.

(6) Eliel, E. L. Conformational Analysis in Heterocyclic Systems: Recent Results and Applications. *Angew. Chem., Int. Ed. Engl.* **1972**, *11* (9), 739−750.

(7) Zeng, F.; Jiang, Y.; He, N.; Guo, T.; Zhao, T.; Qu, M.; Sun, Y.; Chen, S.; Wang, D.; Luo, Y.; Chu, G.; Chen, J.; Sun, S. G.; Liao, H. G. Real-Time Imaging of Sulfhydryl Single-Stranded DNA Aggregation. *Commun. Chem.* **2023**, *6* (1), 1−8.

(8) Murphy, M. C.; Rasnik, I.; Cheng, W.; Lohman, T. M.; Ha, T. Probing Single-Stranded DNA Conformational Flexibility Using Fluorescence Spectroscopy. *Biophys. J.* **2004**, *86* (4), 2530−2537.

(9) Glotzer, S. C.; Solomon, M. J. Anisotropy of Building Blocks and Their Assembly into Complex Structures. *Nat. Mater.* **2007**, *6* (8), 557−562.

(10) Bloomfield, V. A. DNA Condensation. *Curr. Opin. Struct. Biol.* **1996**, *6* (3), 334−341.

(11) Schlenoff, J. B. Zwitteration: Coating Surfaces with Zwitterionic Functionality to Reduce Nonspecific Adsorption. *Langmuir* **2014**, *30* (32), 9625−9636.

(12) Kilinc, V.; Hayakawa, R.; Yamauchi, Y.; Wakayama, Y.; Hill, J. P. Nanoporous Dna Field Effect Transistor with Potential for Random-Access Memory Applications: A Selectivity Performance Evaluation. *Adv. Sens. Res.* **2024**, *3* (5), 2300176.

(13) Zhang, X.; He, N.; Zhang, L.; Dai, T.; Sun, Z.; Shi, Y.; Li, S.; Yu, N. Application of High Intensity Focused Ultrasound Combined with Nanomaterials in Anti-Tumor Therapy. *Drug Delivery* **2024**, *31* (1), 2342844.

(14) Chang, M.; Hou, Z.; Wang, M.; Li, C.; Lin, J. Recent Advances in Hyperthermia Therapy-Based Synergistic Immunotherapy. *Adv. Mater.* **2021**, *33* (4), 1−29.

(15) Bauer, D. W.; Huffman, J. B.; Homa, F. L.; Evilevitch, A. Herpes Virus Genome, the Pressure Is On. *J. Am. Chem. Soc.* **2013**, *135* (30), 11216−11221.

(16) Bauer, D. W.; Li, D.; Huffman, J.; Homa, F. L.; Wilson, K.; Leavitt, J. C.; Casjens, S. R.; Baines, J.; Evilevitch, A. Exploring the Balance between DNA Pressure and Capsid Stability in Herpesviruses and Phages. *J. Virol.* **2015**, *89* (18), 9288−9298.

(17) Spruijt, E.; Sprakel, J.; Lemmers, M.; Stuart, M. A. C.; Van Der Gucht, J. Relaxation Dynamics at Different Time Scales in Electrostatic Complexes: Time-Salt Superposition. *Phys. Rev. Lett.* **2010**, *105* (20), 1−4.

(18) Drobot, B.; Iglesias-Artola, J. M.; Le Vay, K.; Mayr, V.; Kar, M.; Kreysing, M.; Mutschler, H.; Tang, T. Y. D. Compartmentalised RNA

Catalysis in Membrane-Free Coacervate Protocells. *Nat. Commun.* **2018**, *9* (1), 1−9.
(19) Estirado, E. M.; Mason, A. F.; Garcia, M. A. A.; Hest Van, J. C. M.; Brunsveld, L. Supramolecular Nanoscaffolds within Cytomimetic Protocells as Signal Localization Hubs. *J. Am. Chem. Soc.* **2020**, *142*, 9106−9111.

https://doi.org/10.1021/acs.chemmater.5c03128
Chem. Mater. 2026, 38, 1968−1979